DOI:
10.1002/adom.202001923

WILEY-VCH

Self-assembled plasmonic coaxial nanocavities for high-definition broadangle coloring in reflection and transmission

Haibin Ni,[1,] Alexey V. Krasavin,[2] Lu Zhang,[1] An Ping,[1] Chao Pan,[1] Jianxin Cheng,[1] Ming Wang,[3] Jianhua Chang,[1*] and Anatoly. V. Zayats[2*]*

Dr. Haibin Ni, Lu Zhang, An Ping, Chao Pan, Jianxin Cheng, Prof. Jianhua Chang
Jiangsu Key Laboratory of Meteorological Observation and Information Processing, School of Electronic and Information Engineering, Nanjing University of Information Science &Technology,
Nanjing 210044, People's Republic of China
Dr. Alexey V. Krasavin, Prof. Anatoly. V. Zayats
Department of Physics and London Centre for Nanotechnology, King's College London, Strand,
London WC2R 2LS, United Kingdom
Prof. Ming Wang
Jiangsu Key Laboratory on Optoelectronic Technology, School of Physical Science and Technology, Nanjing Normal University, Nanjing 210023, People's Republic of China
E-mail: nihaibin@nuist.edu.cn; jianhuachang@nuist.edu.cn; a.zayats@kcl.ac.uk

Keywords: high-definition angle-independent colors, coaxial nanocavities, nanoapertures, localized surface plasmon

Abstract: Resonant spectral scattering from metallic nanostructures is an attractive alternative approach to produce colors instead of using chemical pigments. In this work, we developed a technological platform based on self-assembled arrays of coaxial plasmonic resonators for generating the bright color gamut over the entire visible spectral range in both reflection and transmission offering the potential for ultra-high definition coloring. Self-assembly approach providing highly efficient mode engineering provides an opportunity to achieve coloring effects over large areas with the local colors being controlled by post-processing. Unlike the approaches using the nanostructure periodicity to define color, the developed method employs the mode engineering based on the localized plasmon resonances in the nanocavities, therefore, providing a broad angular response and viewing angles of up to 40°. With the nanoscale dimensions of the proposed color pixels and increased viewing angular range, the proposed approach allows to achieve large-area color patterns with local coloring controlled by postprocessing important for anticounterfeiting and artistic applications.

1. Introduction

Color definition employing resonant spectral properties of metallic nanostructures related to the excitation of surface plasmons have shown a strong potential for the realization of high-density environmental-friendly displays with long working lifetimes. [1] Different from conventional pigments with ink-spot sizes of around ~20 μm and a print resolution of around 1,000 dots per inch (DPI) and extending already impressive capabilities of all-dielectric approaches, [2] plasmonic nanostructures can confine visible light into subwavelength dimensions, and hence offer an opportunity to dramatically decrease the pixel size and achieve higher DPI, as well as tunable colors. [3] Approaches for plasmonic color formation can be divided into two families: one relying on periodicity of nanostructures and another employing resonances of individual nanostructures. [3c] The former includes wavelength-selective transmission through nano-hole or nano-slit arrays, and resonant interaction of light with arrays of coupled nanoparticles and metal-insulator-metal nano-structures. [4] In this case, the obtained coloring is angle-dependent and a certain number of periods is needed to achieve the effect, therefore, requiring pixel sizes of a few micrometers, despite the arrays are made of sub-wavelength elements. [3a, 3c, 4c, 5] The latter approach is usually realized employing small isolated metallic nanoparticles, which plasmonic resonances and, therefore, the spectral response and the produced colors depend on their size, shape and material composition. [3b, 3c, 6] In this case, the pixel size can be ultimately small being defined by the size of the nanoparticle and seen as a diffraction limited spot, but the intensity of light scattered by individual nanostructures is usually not strong enough to be clearly seen in the bright-field, especially when they are deposited directly on a transparent substrate. [3b, 7] The introduction of a back-reflector below the nanoparticles helps to increase the scattering efficiency in reflection sacrificing coloring in transmitted light. In this geometry, various nanocavity-based plasmonic antennas, such as nanodisks on a film, [1a, 3b] MIM nanocavities with varied

insulator gaps, [8] nanorod and nanotrench structures [9] have been demonstrated with ultimately small pixel size leading to image resolution more than 100,000 DPI, broad and bright color gamut together with high tolerance to the viewing angle. [10] Utilizing the combined action of specular and diffused reflections, the capabilities of nanostructured plasmonic surfaces were further extended to introduction of 3D effects. [9a, 11] Engineering the phase of the reflected or transmitted light opens up the possibilities for its spatial control and the realization of flat lenses, deflectors or holograms. [12]

Self-assembly methods have significant advantages over the low-throughout electron beam lithography-based techniques, allowing fabrication of large areas of nanostructures at low cost. In terms of color definition, the self-assembled nanostructures have so far either low resolution (being based on periodicity or randomization) [13] or offer a very limited color. [14] In this work, we employ the self-assembly fabrication based on the nanosphere lithography to demonstrate engineering of the multiple plasmonic resonances in metal coaxial nanocavities and nanoapertures, covering the entire color spectrum in reflection and transmission. The underlining mode engineering approach based on cylindrical surface plasmons in the coaxial nanostructures increases the absorption efficiency and ensures robust color definition over a broad angular spectrum of illumination and observation. The nanoscale dimensions of the proposed color pixels seen as diffraction limited spots to the observer allow to achieve large-area color patterns with local coloring controlled by postprocessing. The applications may range from high density data storage to anticounterfeiting and artistic designs.

2 Nanostructure design and principle of operation

2.1 Coaxial nanocavity array

Schematic diagram of the coaxial nanocavities with varied geometry and spectral response are shown in **Figure 1**. Coaxial nanocavity arrays were fabricated by the nanosphere lithography

(see Methods for the details). Polystyrene (PS) latex nanospheres were self-assembled into a highly-ordered hexagonal array on a silica substrate, followed by partial etching of the latex spheres using reactive ion etching (RIE). An Ag film was then deposited on the top of the structure to produce an array of nanocavities (Figure 1c). The subwavelength size of the nanocavities (diameter in the range of 10-60 nm) ensures that the ultimate observed pixel size is diffraction limited. Each nanocavity in the array is formed by a dielectric ring protruding into the metal film and act as a resonator selecting frequency of the coupled light. The resonant frequencies, defined by the geometrical parameters of the structure, determine the spectrum of the reflected light (transmission is negligible in this case). Particularly, the spectral response is defined by the excitation of cylindrical surface plasmon (CSP) resonances on both inner and outer walls of the cylindrical nanocavity. [15] When the gap width *W* is decreased to tens of nanometers, as it is realized in the studied nanostructures, the CSP resonances become coupled to produce a gap MIM-type cylindrical mode (g-CSP). [16] While the surface plasmon mode in each nanocavity can be treated as localized mode, the structure can also support delocalized surface plasmon polaritons (SPPs), particularly the SPP Bloch modes (SPP-BW), when the arrays are highly ordered at long distances, e.g., larger than 20 μm.

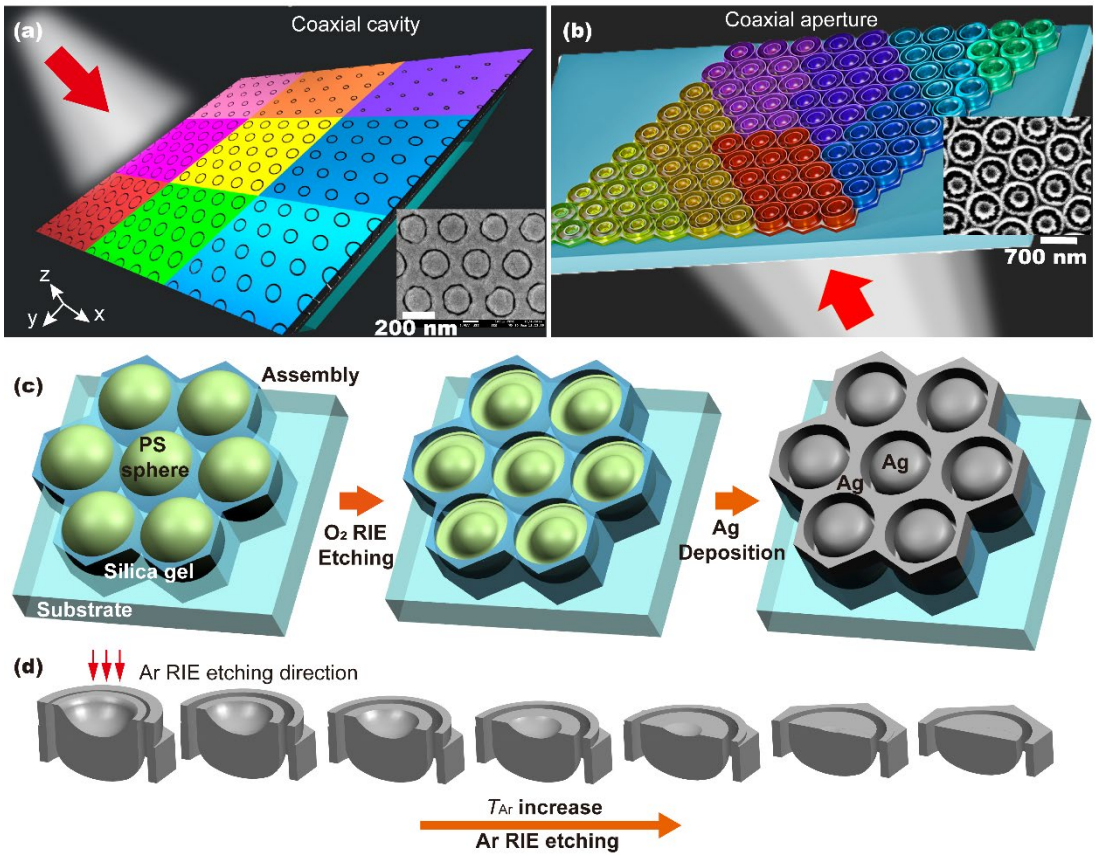

Figure 1. (a) Schematic diagram of the coaxial nanocavity arrays with various parameters producing coloring. Insert: An SEM image of the coaxial nanocavity array with R = 100 nm, W = 10 nm, H = 100 nm, d = 70 nm, P = 250 nm (compare with the final fibrication stage in (c)). (b) Schematic diagram of the coaxial nanoaperture arrays. Inset: An SEM image of the nanoaperture array with R = 280 nm, W = 100 nm, H = 150 nm, d = 100 nm and P = 690 nm (compare with unit cell images at short T_{Ar} times in (d)). (c) Schematic of the fabrication process workflow for the coaxial cavity array. (d) Morphology evolution of the coaxial nanoaperture under Ar milling with increasing time T_{Ar}. Red arrows indicate RIE milling direction. See Methods for details.

2.2 Coaxial nanoaperture array

Besides engineering colors in reflection, color management in a transmission mode is also widely used in displays, filters and windows. [17] To address these applications, coaxial nanoaperture arrays with high transmission can be produced from their coaxial nanocavity counterparts (see Methods for details), preserving the CSP-based optical properties and hence providing tunable colors in the transmission mode. To achieve this, the coaxial nanocavity

arrays were coated with a layer of polyurethane (PU) polymer and peeled off from the substrate. Then, the PU film was turned upside down and glued to another glass slide. Finally, the sample was milled using RIE to form the coaxial nanoaperture array. Depending on the milling degree, which changes the height of the coaxial nanocavity, the resulting structure exhibits different colors, as illustrated in Figure 1b,d.

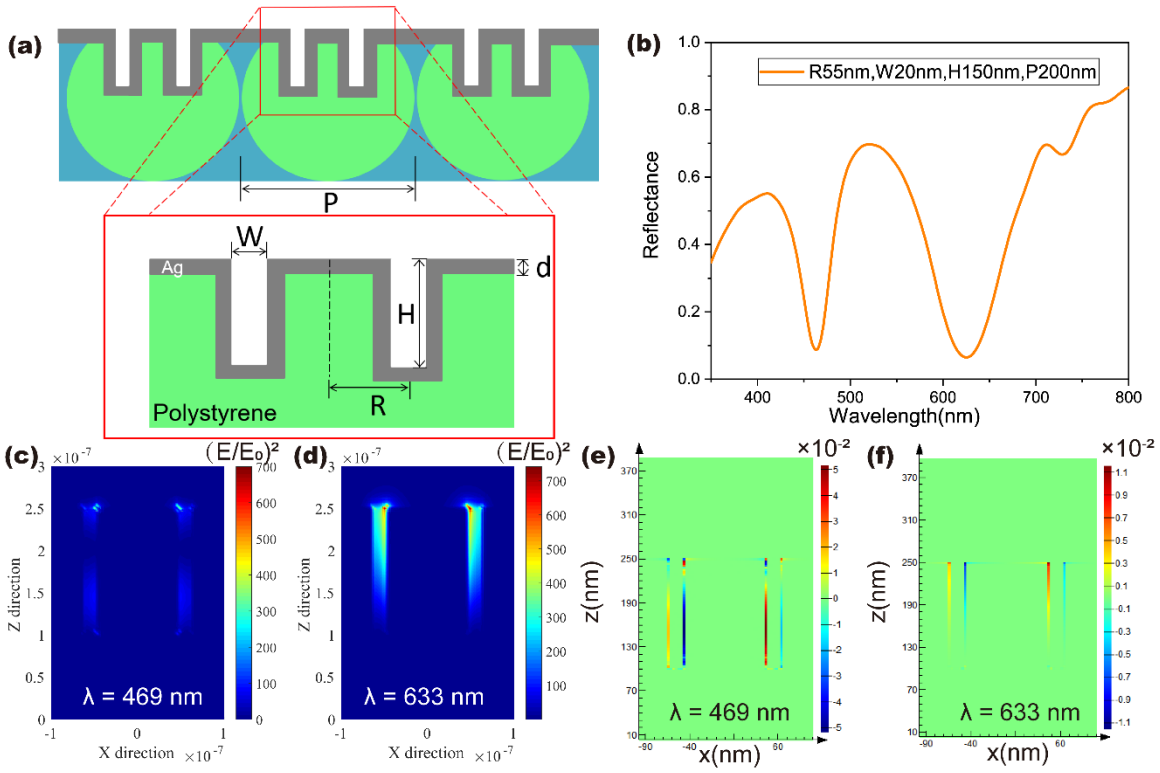

Figure 2. (a) An idealized unit-cell cross-section of coaxial nanocavities with indicated geometrical parameters. (b) Typical simulated reflection spectrum of a coaxial nanocavity array with R = 55 nm, W = 20 nm, H = 150 nm and P = 200 nm. (c,d) Electric field intensity and (e,f) charge distributions in *xz*-plane at 469 nm and 633 nm wavelengths, corresponding to the reflection dips in (b).

2.3 Principle of color definition

Geometrical parameters of the coaxial nanocavity R, W, and H (shown in **Figure 2**a), as well as composition materials determine the resonant frequencies of the supported g-CSP modes

and therefore the color of light reflected from the nanocavity arrays or transmitted through the coaxial nanoaperture arrays. [18] The excited g-CSP modes (Figure 2b) are characterized by highly enhanced electric field in the coaxial gaps (Figure 2c–f). Upon illumination, the g-CSP modes that satisfy boundary conditions in the axial and azimuthal directions of the coaxial nanocavity are excited. Particularly, the g-CSP mode should fulfill a Fabry-Perot-type phase matching condition in the axial direction:

$$\left|2Hk_{\mathrm{g-CSP}}(\omega) + \Delta\theta_1 + \Delta\theta_2\right| = 2\pi m, \quad (1)$$

where $\Delta\theta_1$ and $\Delta\theta_2$ are the phase changes upon the mode reflection at the top and bottom interface, respectively, $k_{\mathrm{g-CSP}}(\omega)$ is the wave vector of the g-CSP mode and m is an integer describing the mode order in the vertical direction. [5g, 18] Beside this relation, the mode should also fulfill azimuthal phase matching condition:

$$2\pi R k_{\mathrm{g-CSP}}(\omega) = 2\pi n, \quad (2)$$

where n is an integer, describing the corresponding mode order. Engineering the dispersion of the g-CSP mode via the variation of the nanocavity/nanoaperture geometrical parameters, resonances at predesigned wavelengths can be achieved. Under the resonant conditions, the light at the prescribed wavelength is strongly absorbed due to the loss in the metal, resulting in the removal of these wavelength from the nanostructure reflection/scattering spectrum and provide the control of the color in both reflection and transmission over the whole visible range.

Delocalized SPP-BW modes may also be exited and supported by the entire array; their optical frequencies are additionally defined by the array periodicity. [19] Together, SPP-BW and g-CSP resonances will determine the finally observed colors. However, for the designed parameters, the coloring is defined by g-CSP modes ensuring angle independent performance and diffraction-limited size of the observed color pixels.

3 Results and discussion

3.1. Experimental color management with coaxial nanocavity arrays in reflection

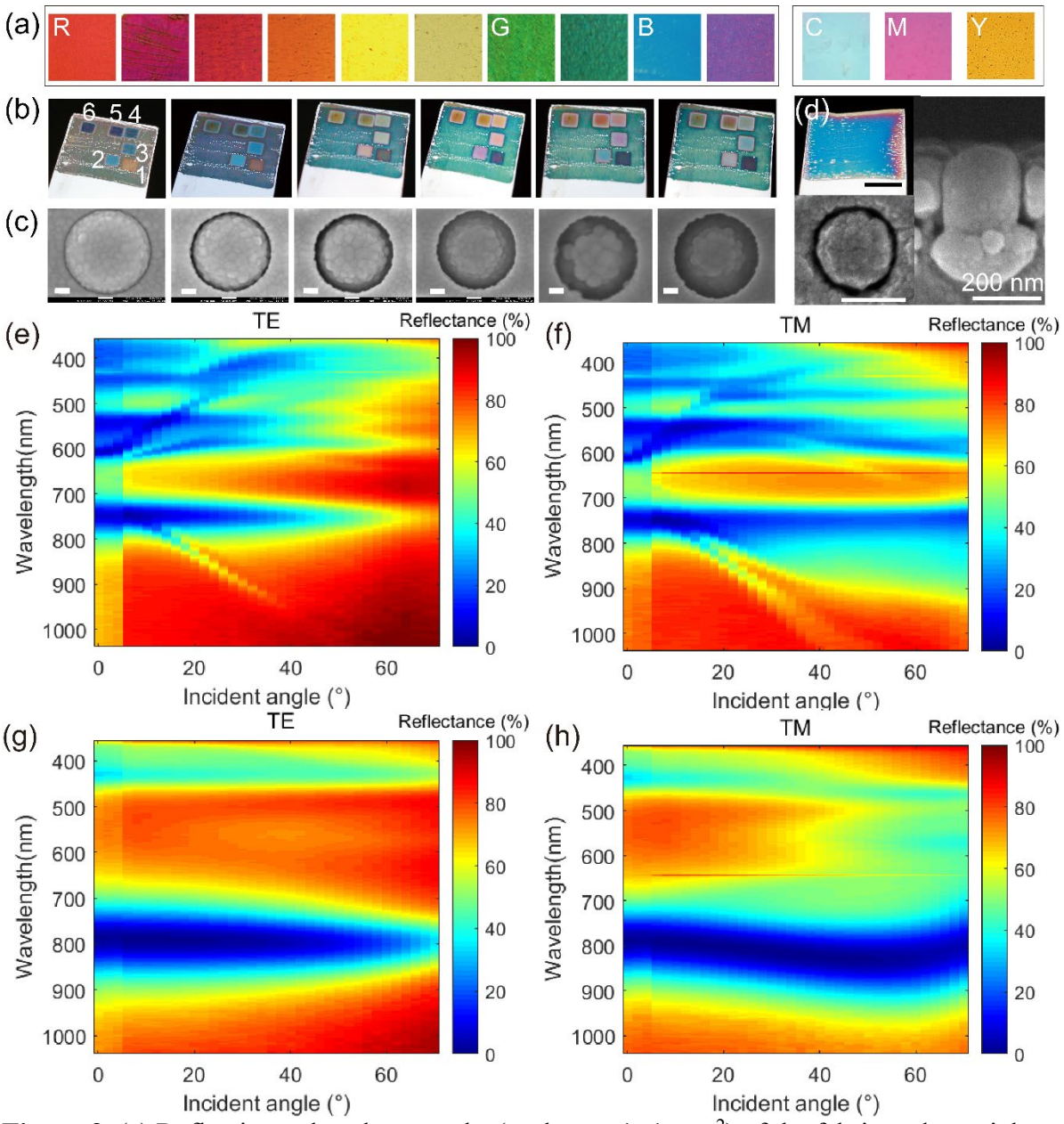

Figure 3. (a) Reflection color photographs (each area 1×1 mm^2) of the fabricated coaxial nanocavity arrays with structural parameters: P = 690 nm, W, H and R are simultaneously varied from 20 to 100 nm, from 100 nm to 400 nm and from 200 nm to 300 nm, respectively, during the fabrication process. (b) Color photographs of six coaxial array areas with various initial states after RIE (marked with 1–6 on the left image) at subsequent stages of silver film deposition (images left to right). The initial geometrical parameters for structures 1–6 in are: 1) R = 325 nm, W = 30 nm and H = 30 nm; 2) R = 310 nm, W = 60 nm and H = 58 nm; 3) R = 295 nm, W = 90 nm and H = 86 nm; 4) R = 280 nm, W = 120 nm and H = 114 nm; 5) R = 265 nm, W = 150 nm and H = 142 nm; 6) R = 250 nm, W = 180 nm and H = 170 nm; which corresponds to a simultaneous variation of the parameters from sample 1 to sample 6 with a step $\Delta R \approx 15$ nm decrease, together with $\Delta H \approx 28$ nm and $\Delta W \approx 30$ nm increases; P = 690 nm is fixed for all 6 samples. Size of each square is 2 mm × 2 mm. Photographs from left to right

demonstrate the coloring of the structures with a continuously increased thickness of a sputtered Ag film d from 25 nm (first image on the left) to 150 nm (last image on the right) in a step of ~ 25 nm, corresponding to simultaneous decreases of ΔR = ~ 6 nm and ΔW = ~ 12 nm and increase of ΔH = ~ 25. (c) SEM images of coaxial nanocavity arrays in areas 1–6 marked in (b) after sputtering 150 nm thick Ag film. Scale bars are 100 nm in all the images. (d) Optical and SEM images of the experimentally produced coaxial nanocavity arrays with R = 105 nm, W = 12 nm, H = 100 nm and P = 250 nm. The scale bar is 5 mm in CCD image and 200 nm in SEM images. (e–h) Experimentally measured angle-resolved reflection spectra (0–70º) of coaxial nanocavity arrays for (e,g) TE- and (f,h) TM-polarized incident light for the samples with structural parameters: (e,f) R = 250 nm, W = 75 nm, H = 375 nm, P = 690 nm, d = 225 nm and (g,h) R = 100 nm, W =15 nm, H = 100 nm, P = 250 nm and d = 70 nm. The abrupt change at 5º is due to an unavoidable minor change of the light spot position at small angles.

Coaxial nanocavity arrays with varied geometry designed using the principles above and produced by the nanosphere lithography over the large areas (at least 10 $\times$10 mm^2) display colors which cover the whole visible range (**Figure3** a–d). Selective oxygen RIE etching with a time T_{O2} defines at an initial fabrication stage R, W, and H parameters for different areas of the sample. Since the color is directly defined by geometry parameters of R, W, H and P, we use the four parameters to define a coaxial cavity while using etching time T_{O2} and metal film thickness d as fabrication parameters. By choosing the thickness d of the deposited Ag film, H, R, and W can be continuously tuned, which results in the change in the reflected colors under the white light illumination (Figure 3b). Morphology evolution of coaxial nanocavities with different initial geometric parameters but with the same metal film thickness (d = 150 nm Ag) clearly indicates to the simultaneous tuning of R, W and H (Figure 3c) by etching time T_{O2} at the previous stage. As etching time T_{O2} increases, R decreases, while W and H increase. Furthermore, H is also partially determined by the thickness of the deposited film. The diameter of the spheres used in the fabrication determines the period of the array P (Figure 3d). One can see that with tuning the geometrical parameters of the nanocavity arrays during the fabrication process, both RGB and CMY color pallets can be realized.

The color of light reflected from the coaxial nanocavity arays is produced by the subtraction of the resonant spectral bands from the white light illumination, therefore, it depends on both magnitudes and wavelength of the resonant reflection. It is controlled by the geometrical parameters and composition materials of the nanostructure. Before investigating the influence of the geometrical parameters on the reflected color, it is important to distinguish the role of g-CSP and SPP-BW modes. Reflecting the localized nature of the excited g-CSP modes, the broad and strong non-dispersive resonances at 450 nm, 560 nm and 750 nm in the angle-resolved reflection spectra (see Methods for the measurement details) (horizontal bands in Fig 3e, f) insure that the produced color will not change with ± 40º variation of the incident and observation angles. In addition to g-CSP modes, much less pronounced dispersive SPP-BW modes, characterized by the narrow line widths and shallow reflection dips (narrow inclined bands in Figure 3e,f), are also present in the reflection spectra, but they have angular dependence being derived by the SPP interference effects. At shorter wavelengths, there are noticeable anti-crossing effects between the localized and propagating modes. At the same time, it is clear that the g-CSP modes dominate the coloring effects, while SPP-BW modes have a negligible effect on the color due to their scattered amplitude, which is needed for angle-independent performance.

Experimentally measured reflection maps show that the structures with shorter periods (Figure 3d) offer better color performance. The decrease of the periodicity to 250 nm can practically eliminate the effect from the SPP-BW modes in the visible by moving the Bloch structure in the direction of shorter wavelengths (Figure 3g,h). Additionally, the viewing angle range can be further increased to more than ± 60º. Moreover, there is only one dominant reflection dip in the visible range for smaller coaxial nanocavities in such arrays, which makes it easy to tune the reflection color. Numerical simulation results further confirm such angle independent properties of the coaxial nanocavities (see **Figure S1**). Due to the

symmetry of the coaxial nanocavities, their spectral response is also independent on the in-plane angle (polarization) at normal incidence (and at least less than 20 degree). Engineering the spectral response through the geometrical parameters of the nanocavities and arranging them in a matrix of pixels one can produce an image or encode the information for the data storage. A defining role in the image resolution or the density of the stored data plays the pixel size, which crucially depends on the physical mechanism underlying the color formation. As in the case of the nanocavities it is related to the excitation of localized g-CSP modes, supported by single structures, each nanocavity can work as an individual pixel. This leads to the possibility of the ultimately smallest pixel size approaching the diffraction limit. With the approach demonstrated here employing 250 nm PS spheres, the resolution of the color display can be achieved more than 100,000 DPI. The resolution of the color image definition also depends on the ability to selectively modify the related geometrical parameters locally. In the proposed approach, several mechanisms can be used to achieve this: i) selective assembly of the PS spheres of different sizes, ii) locally selective RIE, or iii) locally selective plasmonic film thickness. Outside self-assembly approach, standard lithography methods or nanoimprint techniques can be used to define g-CSP cavities. Implementation of a multi-color pixel array via tuning the geometrical parameters of the nanocavities through selective etching (followed by the usual Ag film deposition) using a 30 μm Cu grid as a mask is demonstrated in **Figure S2**a. In addition, the ultimate resolution down to the size of a single nanostructure is presented in Figure S2b,c.

3.2 Numerical optimization

Numerical simulations were used to further analyze the experimental findings and reveal the full potential of the proposed approach (see Methods for the details of the numerical simulations). Good agreement with the experimental results for P = 250 nm (**Figure S3**) was obtained, ensuring the feasibility of the numerical approach, and then detailed study of the

spectral response was carried on. As it follows from the nature of coaxial waveguide modes (Eqs. 1,2), the resonant reflection dip continuously shifts to longer wavelength with the increase of R (**Figure 4**a) or H (Figure 4b) and the decrease of W (Figure 4c). Particularly for a period P = 250 nm with the radius R increase from 15 to 65 nm, the reflection dip shifts in a very broad range from 380 nm to 650 nm, spanning the whole visible spectral range (Figure 4a). This gives the possibility to continuously vary the desired pixel color in the CMY gamut (Figure 4e). As was mentioned above, in practice the variation of the radius can be achieved by choosing the PS spheres of various diameters for the self-assembly and be further fine tuned by the thickness of deposited film. The same effect of scanning the reflection color can be achieved by varying the gap width W (Figure 4c), which can be controlled during the fabrication by choosing the etching time T_{O2} or the thickness d of the metallic film. It is interesting to notice that the width of the reflection dip is relatively constant as R and H are varied (Figure 4a,b), while the dip broadens as W increases or P decreases (Figure 4c,d), most probably resulting from the fact that the resonances in the neighboring nanocavities become coupled, with the decrease of the separation in the latter case and with the increase of out-of-nanocavity leakage in the former.

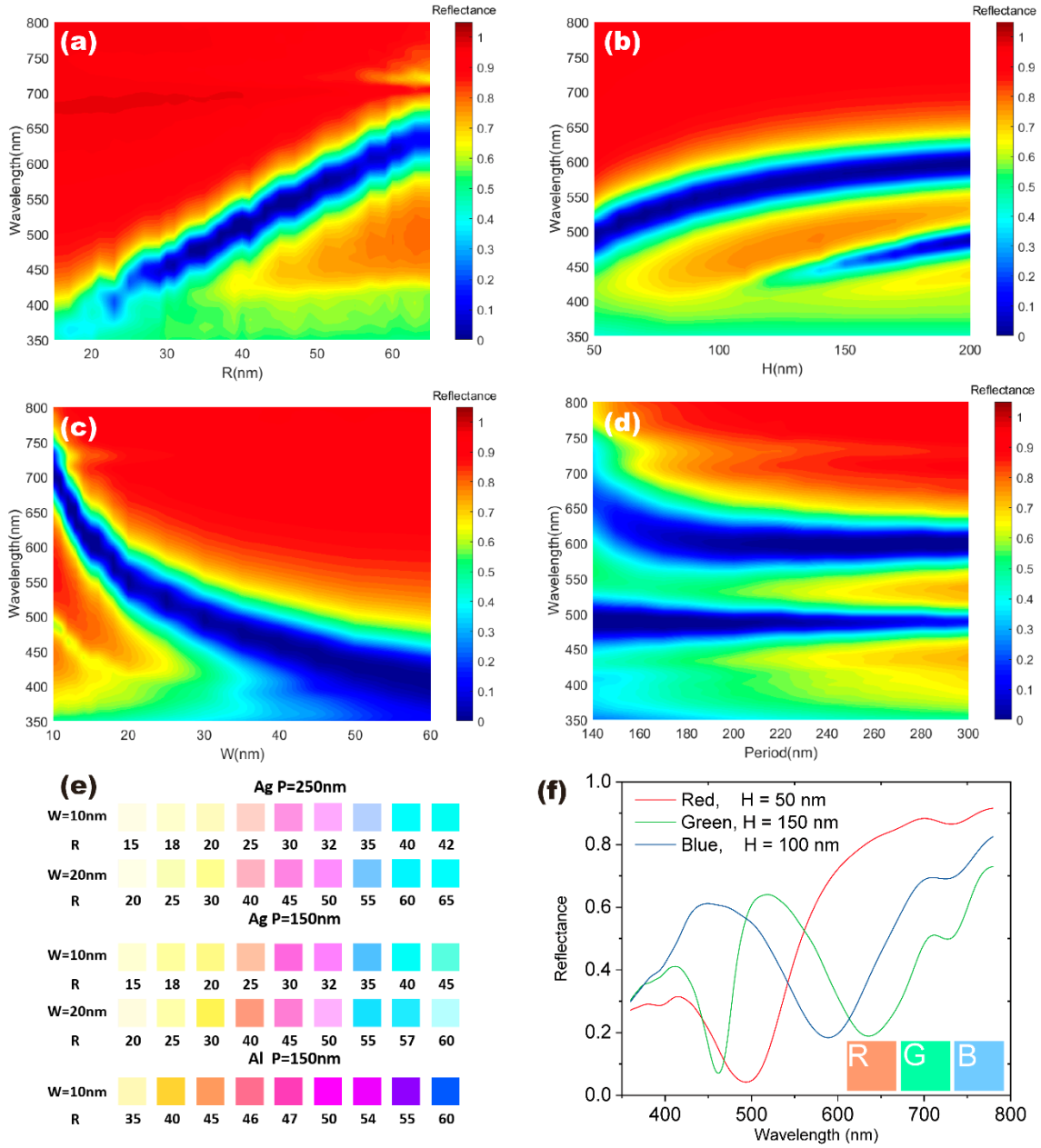

Figure 4. Numerically simulated reflection spectra for (a-d) different (a) radia *R,* (b) heights *H,* (c) gap widths *W* and (d) periodicities *P* for the coaxial nanocavity arrays in an Ag film. The fixed parameters (set of three in each case) in (a–d) are $R = 50$ nm, $W = 20$ nm, $H = 100$ nm and $P = 250$ nm except for (d) where $H = 200$ nm. (e) CMY color pallet produced by the color of coaxial nanocavity arrays with varied *R, W* and material composition, but with same $H = 100$ nm, obtained using numerical simulations (see Methods). (f) RGB color pallet realized by varying the nanocavity height *H* with the corresponding reflection spectra $W = 20$ nm, $R = 51$ nm and $P = 150$ nm.

The evolution of the numerically simulated reflection spectra was transformed into colors according to the CIE 1931 *xy* color space chromaticity diagram (see Methods for the details).

As the result, with the change of a single geometrical parameter *R* and the properly engineered design, the coaxial nanocavity arrays practically demonstrate tuning of the reflected color from yellow to red and then to blue (Figure 4e). When *W* decreases from 20 nm to 10 nm, similar colors can be reproduced, again by only varying the radius *R*, which indicates that colors reflected from coaxial nanocavities have high tolerance to the variation of the smallest nanostructure parameter (*W*) and, therefore, have broad allowances for the fabrication process. Periodicity *P* does not change the color dramatically as it changes from 250 nm to 150 nm. Even with a different plasmonic material (Al, which additionally is abundant and cheap), the coaxial nanocavity arrays still show a similar color evolution but with a minor difference attributed to the material properties as will be discussed below. Due to the subtractive nature of the colour formation, the CMY gamut is naturally and controllably reproduced by the nanocavity arrays through the excitation of individual absorptive plasmonic resonances. The RGB color gamut, on the other hand, is generally based on emissive colors. However, it is possible to achieve RGB-type pallet with absorptive plasmonic resonances or their collective action, producing broad absorption bands. For example, in order to reproduce red colour in reflection, light in the visible spectral range should be absorbed except the red wavelengths. In a similar manner, a blue colour in reflection can be obtained. To realize a green colour, two absorption resonances are needed in order to eliminate the visible light in the short- and long-wavelength spectral ranges with respect to the green one. **Figure S4** shows the realization of the RGB pallet using a nanocavity array with $P = 200$ nm. A full scan of the spectral response in the *R*-*H* parameter space performed for a smaller period $P = 150$ nm shows that the RGB gamut can be reproduced with a change of a single parameter *H* at $R = 51$ nm and $W = 20$ nm (Figure 4f), which is experimentally feasible. This is achieved taking the advantage of a continuous shift of a broad plasmonic resonance through the entire visible spectrum, initially absorbing all the

wavelengths except red, then except blue, and, finally, with a further increase of H, the appearance of a higher-order plasmonic resonance in the short-wavelength range, additionally blocking blue again (Figures S4 and S5). Overall, the experimentally measured (Figure 3) and numerically calculated (Figures 4 and S5a) spectral dependences agree with each other and show that the efficiency of coupling of the incident light to plasmonic resonances can reach values much higher than 90% (corresponding to less than 10% reflection), with a baseline reflection level of 70%.

Finally, the localized nature of the g-CSP modes was confirmed in numerical investigation of the reflection spectrum as a function of the period. As illustrated in Figure 4d, the positions of both reflection dips do not shift with the variation of *P* from ~180 nm to 300 nm, signifying the fact that the transmission spectrum and, therefore, the encoded color are efficiently defined by the properties of the individual nanocavities (the slight spectral shift of the long-wavelength resonance at smaller periods is most probably related with the onset of coupling on the neighboring modes). This will be further confirmed by the simulation results for an isolated coaxial nanocavity. The reflection dips corresponding to the excitation of the localized g-CSP modes keep the same wavelength positions as in the case of the array, though experiencing a decrease in the magnitude (**Figure 5**a).

3.3 Random nanocavities

As some coupling between the localized modes in the nanocavities was observed when they are closely packed in ordered array, signified by the broadening of the dips in Figure 4c,d as well as the slight shift of one resonance in Figure 4d, more insight into the effect can be gained investigating the color generated by randomly located coaxial nanocavities. Simulated reflectance spectra of such structures with an average distance between the nanocavities around 300 nm, 200 nm and 100 nm are presented in Figure 5b. For a fair comparison all nanostructures had 7 nanocavities and the reflection in all three cases was normalized to the

light power incident on a 1.5 μm×1.5 μm area. Similarly to the effect observed in the periodic arrays, when the distance between neighbor nanocavities becomes lower than 200 nm, coupling between the nanocavities grows stronger characterized with slight broadening of the reflection dip with no change in the dip position, which overall produces only a minor change in the observed color (Figure 5b). On one hand, it further confirms the robust behavior of the localized g-CSP modes in respect to changing the distances between nanocavities and on the other hand it demonstrates the stability of the developed approach in respect of color encoding even with randomly distributed coaxial nanocavities, thus, tolerances in the fabrication process.

3.4 Material dependence

Besides using silver as the plasmonic material, we further calculated the colors reflected from the same coaxial nanocavity arrays in an aluminum film (Figure 5c), as this material is abundant and the structures made from it are more stable. [20] The aluminum arrays showed similar evolution with the single reflection dip spanning through the entire visible spectral region with the change of the nanocavity radius, which demonstrates the mass-production potential of the approach (Figure 4e). The linewidth of the resonant reflection dip is another important factor that affects the resulting color. The linewidth of a surface plasmon resonance, underlying it, is determined by both Ohmic and radiation losses, which can be presented by the relation $1/\tau_{tot} = 1/\tau_{ohmic} + 1/\tau_{rad}$, where τ_{tot}, τ_{ohmic}, and τ_{rad} are the total decay time and the decay times corresponding to Ohmic and radiation losses, respectively. Thus, in addition to the shape and the geometrical parameters of the structure, τ_{ohmic} and τ_{rad} are other parameters that can be tuned through the change of the plasmonic material, which affects both loss experienced by the mode and its radiation properties through the material optical constants.

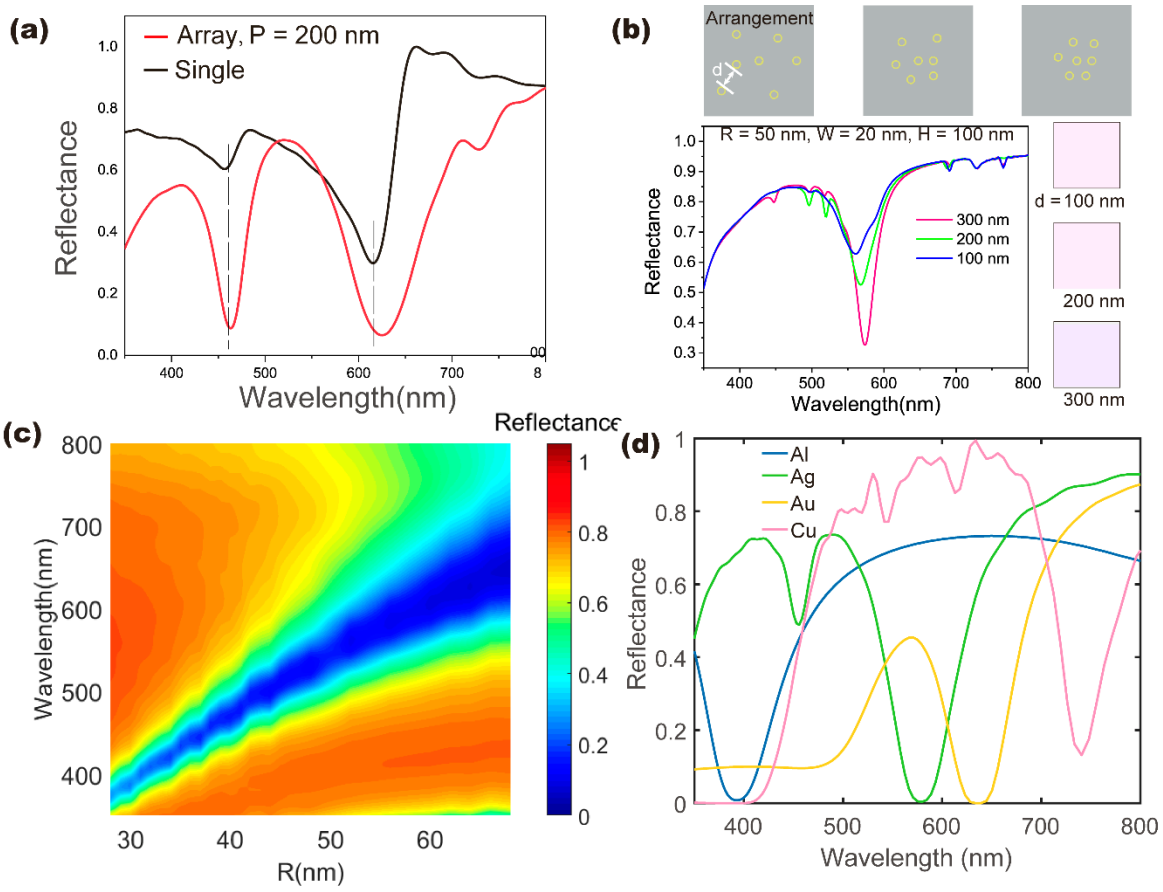

Figure 5. (a) Comparison between the numerically simulated reflection spectra of periodic Ag coaxial nanocavity array (R = 55 nm, W =20 nm, H=150 nm, P = 200 nm) and a single coaxial nanocavity with R = 55 nm, W =20 nm, H=150 nm. (b) Schematic diagram of coaxial nanocavities located at random positions with average distances about 300 nm, 200 nm and 100 nm, together with numerically simulated reflection spectra of the random arrays presented in the top line. On the basis of the simulated spectra, the colors in the left bottom were obtained. (c) Color management using Al coaxial nanocavity arrays with R = 28–68 nm, W = 8 nm, H = 100 nm and P =250 nm; (d) Numerically simulated reflection spectra of the coaxial nanocavity arrays with the same R = 35 nm, W = 10 nm, H = 100 nm, P = 150 nm realized with various metallic materials.

Coaxial nanocavities made from other plasmonic materials were also numerically studied (Figure 5d). Various optical properties of these materials (both plasma frequencies and the presence/position of inter-band transitions) provide the opportunity to engineer the reflected colors using the material-related degree of freedom. For example, using aluminum-based arrays it is possible to produce a deeper blue color due to a broad and steep reflection dip across a 500 – 720 nm range (Figure 4e).

3.5 Dependence of reflected colors on fabrication tolerances

It is inevitable that there will be discrepancies between the nominal design and the real fabricated samples in terms of a change of the nanostructure geometry present in all the nanostructures (characteristic to the fabrication method) and the variation of the geometry among the structures, leading to a certain spread of geometrical parameters in the assembly. All of this can affect the optical performance of the array. Having in mind prospective fabrication of the samples by a nanoimprint method, the color tolerance of the coaxial nanocavity arrays was evaluated in terms of the unintended variation of the gap width, characteristic to this technique. Keeping the nominal radius *R* and bottom width *W* constant, the gap width was increased towards the top decreasing the internal radius *r*, varied from 45 nm, corresponding to the nominal structure with vertical walls, to 35 nm. In such non-cylindrical nanocavities, both resonances in the reflection spectrum (designed to produce a green color) experience a shift of around 50 nm (**Figure** 6). Although there is a noticeable color evolution, it can be accounted for by changing the nominal geometrical parameters to adjust for the particular characteristics of the implemented nanoimprint process.

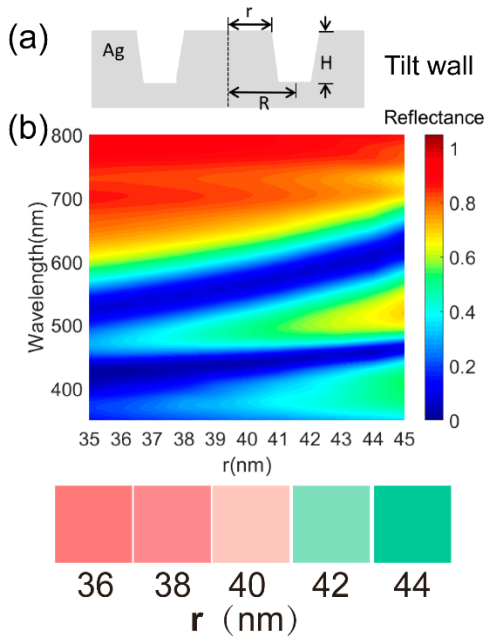

Figure 6. (a) Schematic cross section of a coaxial nanocavity having tilted side walls; (b) Reflection spectra as a function of the inner radius of the coaxial nanocavity *r* (indicated in

(a)), varied from 45 nm (vertical walls) to 35 nm (4°tilted walls) with R = 55 nm, W=20 nm, H = 150 nm, P = 200 nm, together with the corresponding reflection colors.

3.6 Color engineering for transmitted light

When the coaxial nanocavities are redeposited upside-down on another substrate and ion-etched from the backside to produce nanoapertures (see Methods for the details), the arrays can also be used to display colors in a transmission mode. SEM images of the fabricated coaxial nanoaperture arrays are presented in **Figure 7**a. The transmitted colors can be defined in the same way through engineering of the plasmonic modal profile of the nanostructure via variation of the nanostructure geometrical parameters, the origin of the plasmonic resonances determining the modal profile remains essentially unchanged. Particularly, the nanoaperture size (depth of the cavity) D was tuned by the variation of the milling time T_{Ar}. As the etching process continues, the slit width W increases and the sample shows a change of color in the transmission mode (Figure 7a–c, f–k). The color variation in transmission is complemented with the corresponding variation in reflection (Figure 7d). Complementing the experimental results, the simulations allow monitoring continuously the structure parameter variations and resulting colors (Figure 7e). The experimentally measured and numerically simulated colors in transmission agree quite well, at the same time the colors in reflection agree at smaller RIE times (12 mins) and larger RIE times (30 mins experimental color agrees with 33 mins simulated color), but disagree in the middle RIE time range (12-18 mins). The reason this is that in numerical simulations it is very difficult to exactly implement the complex evolution of the nanostructure geometry during the RIE etching, including the geometry of the nanoaperture shallow inner cavity.

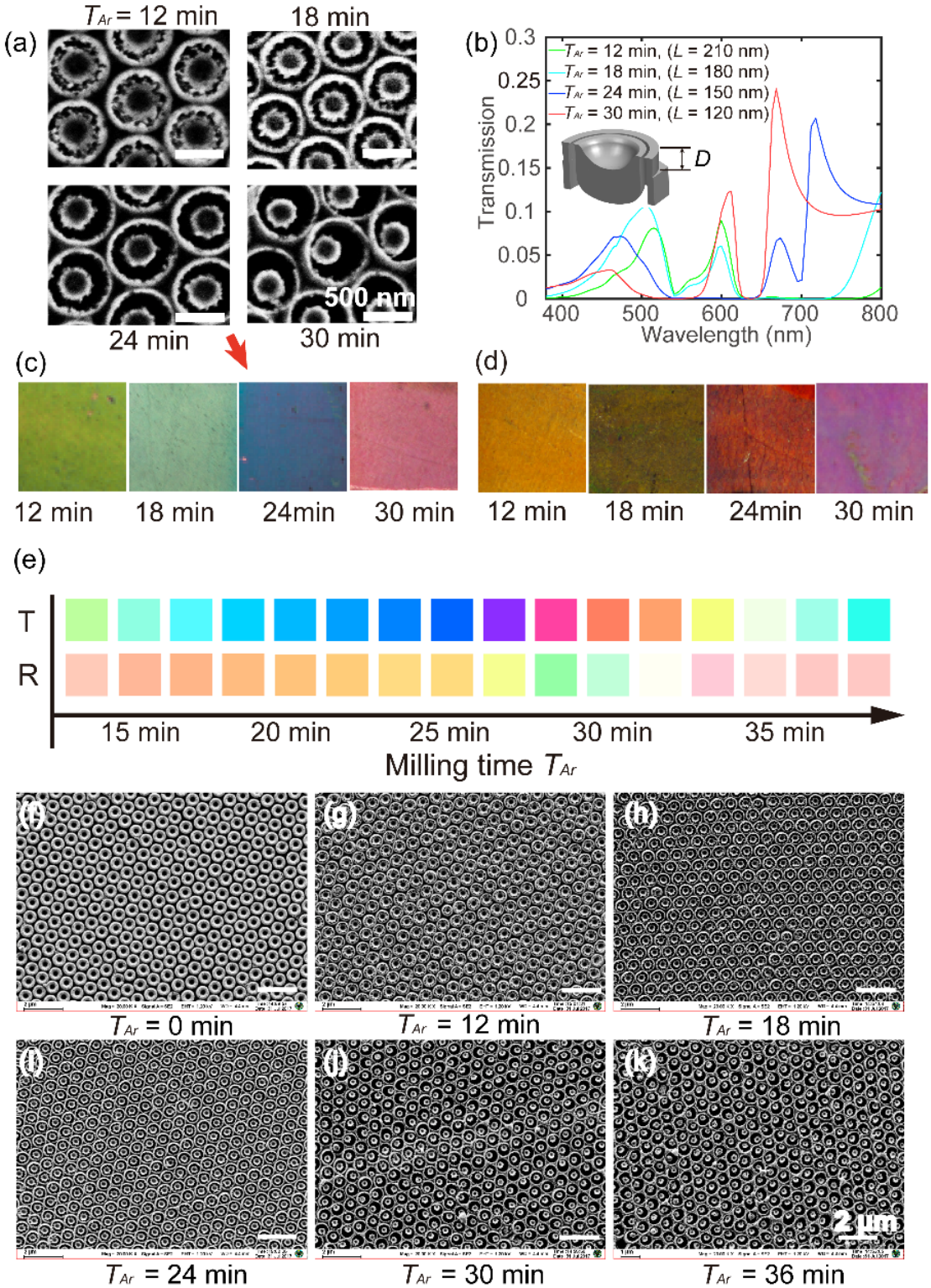

Figure 7. (a) SEM images of the coaxial nanoaperture arrays with an increasing gap width. Scale bar is 500 nm in all images. (b) Simulated transmission spectra of the coaxial nanoaperture arrays (R = 210 nm, W = 160 nm, D =270 nm, P = 690 nm) after various milling times (leading to the decrease of D), calculated for etching speed of ~5 nm/min. The inset shows the geometry of the cross section of the coaxial nanoaperture. Transmission (c) and

reflection (d) images of the coaxial nanoaperture arrays for milling times varied left-to-right: 12, 18, 24 and 30 min. The size of the squares is 2×2 mm^2. (e) Colors of the coaxial nanoaperture arrays in transmission and reflection obtained from numerical simulations. (f–k) SEM images showing the evolution of the nanostructure array during the milling process: (f) initial backside surface morphology of the coaxial nanocavity array, as it is peeled off from the glass substrate, (g–k) after T_{Ar} = 12 (g), 18 (h), 24 (i), 30 (j) and 36 (k) minutes of the reactive ion etching. Scale bar is 2 μm.

4 Conclusion

Bright coloring spanning through the entire visible spectral region both in reflection and transmission was obtained engineering the plasmonic modes of the self-assembled arrays of coaxial nanocavities and nanoapertures through the straightforward variation of their geometrical parameters at the fabrication stage. The color encoding based on localized plasmonic modes in individual nanostructures offers the prospective to realize pixels of ultimately small sizes approaching the diffraction limit, potentially providing ultra-high pixel density and display resolution of 100,000 DPI. Furthermore, due to this mechanism the color response of the proposed nanostructures remains the same with the variation of the illumination and observation angles up to at least 50°, ensuring a large display viewing angle. The definition of both CMY and RGB color pallets as well as many intermediate colors has been demonstrated. The implemented fabrication method allows high quality and large area manufacturing at a low cost. Overall, the proposed approach can be applied to realize high contrast, high resolution color displays, [21] high density information storage, [22] colorimetric sensors, [23] image encryption, [24] and engineering of reflected or transmitted spectra. [25]

5. Methods

Fabrication of coaxial nanocavity arrays: Monodisperse colloidal particles (polystyrene latex, nominal diameter d = 250 nm or 690 nm, polydispersity <10% from Bangs Laboratories Incorporated, used as received) were suspended uniformly in a water solution. Standard glass slides were cleaned with a 3:7 volume ratio solution of H_2O_2:H_2SO_4 for 1 h at 90°C, which

was followed by rinsing with DI water and drying with N_2 gas. The slides were treated with an oxygen plasma (Harrick Plasma Cleaner, PDC-002) under mild conditions for 10 min before use. Six mL of DI water were added to the 20 μL polystyrene (PS) microsphere suspension with a sphere diameter of 690 nm and a 20 μL of hydrolyzed TEOS solution (98%, Sigma Aldrich). The resulting solution was sonicated for 5 min at room temperature to form the suspension for the assembly. The TEOS solution consisted of a 1:1:1.5 weight ratio of TEOS (98% Aldrich), 0.1 M HCl, and ethanol (99.9%) and was stirred at room temperature for 1 h prior to use. [26] A cleaned glass slide was partly vertically immersed into the mixed suspension and fixed. Then, the suspension was placed in an oven for evaporation at a temperature of 45°C ± 1°C. After the suspension was evaporated, a monolayer of ordered sphere arrays infiltrated with a silica gel was formed on the slide. For PS spheres of a 250 nm diameter, the concentrations of the spheres and TEOS solution, as well as the evaporation temperature need to be slightly adjusted to form high quality monolayer sphere arrays.

The samples with the ordered sphere arrays infiltrated with the silica gel were treated with reactive ion etching (RIE) with O_2 to achieve selective etching of the PS spheres. An Ag film (0.025 Torr, Ar, 2.5 sccm) was deposited on the sample at a rate of ~ 0.4 nm/s by magnetron sputtering (Jiashuo Vacuum Technology), the film thickness was monitored by a quartz oscillator. A 300 μm-thick Al_2O_3 slide (with a 2 mm × 2 mm square opening aperture) was used as an RIE etching mask for selective etching of the monolayer of the ordered sphere array. The process gradually etches the nanospheres producing the nanocavity structures, the etching time can be varied to achieve the nanocavities with the desired geometrical parameters (Figure 1b). Morphology of the fabricated samples was characterized by scanning electron microscopy (JSM 7610F, JEOL). A thin layer of a Pt film was sputtered on the samples to increase the conductivity of the sample surface prior to the SEM characterization.

Fabrication of coaxial nanoaperture arrays: Coaxial nanocavity array was made by the method described in the previous section using 15 min O_2 etching and a 150 nm Ag film. Then, a 1 mm thick layer of NOA61 was coated on the top of the array and fully cured by UV light for 2 min. After this, the cured NOA61 film together with the Ag coaxial nanocavity arrays was peeled off from the substrate. RIE milling was used for etching the back side of the coaxial nanocavities to form coaxial nanoapertures. The etching parameters were: Ar, 20 sccm, pressure reactor 10 Pa, 60W RF power. The etching times were 12, 18, 24 , 30 and 36 min, respectively. A 30 μm Cu mesh with grid size of 120 μm was used as RIE etching mask to selectivly etching the sample to produce patterns of color.

Spectral characterization: Reflection spectra of the coaxial nanocavity arrays from 360 to 800 nm were measured by an optical spectrum analyzer (OSA, Ocean optics, USB 2000, 360–1100 nm) equipped with a 200-μm-core diameter reflection probe (Ocean Optics). A white light source (Yokogawa AQ4305, 50W) was coupled to six fibers in the reflection probe and was normally projected onto the surface of the coaxial nanocavity arrays, the reflected light was collected by another fiber in the bunch and sent to the OSA for detection. The measurements of angle resolved spectra of the coaxial nanocavity arrays were performed using the R1 device (Fuxiang Optics).

Simulation: Reflection and transmission spectra, electric field and charge density distributions were simulated using an FDTD method (Lumerical solution). Periodic boundary conditions were applied in the lateral directions, while in the direction perpendicular to the array perfectly matched layers (PMLs) were used. In the situations of a single nanostructure, PMLs were applied in all the direction. Mesh size in all simulations was set to be 2 nm.

Color transformation: The 1931 CIE standard color space was used to transfer the simulated spectral response of the coaxial nanostructures into the produced colors. From the spectral

power distribution I of the reflection spectra, XYZ values of the CIE can be determined using the formulas:

$$X = \int_0^\infty I(\delta)\bar{x}(\delta)d\delta, \quad (3)$$

$$Y = \int_0^\infty I(\delta)\bar{y}(\delta)d\delta, \quad (4)$$

$$Z = \int_0^\infty I(\delta)\bar{z}(\delta)d\delta. \quad (5)$$

In the XYZ parameter set of the CIE color space, Y indicates the brightness, and X and Z define the color itself. Thus, a CIE xy chromaticity graph is usually used to represent the obtained color map, where the coordinates x and y are calculated as

$$x = \frac{X}{X+Y+Z}, \quad (6)$$

$$y = \frac{Y}{X+Y+Z}. \quad (7)$$

Supporting Information

Supporting Information is available from the Wiley Online Library or from the author.

Acknowledgements

H. N. would like to thank National Natural Science Foundation of China (Grants 61605082 and 61875089), the Natural Science Foundation of Jiangsu Province (BK20160969, BE2016756), and the Priority Academic Program Development of Jiangsu Higher Education Institutions (PAPD). China Postdoctoral Science Foundation Funded Project (2017M611654). A.V.Z. and A.V.K. acknowledge the support from EPSRC UK (EP/M013812/1) and ERC iCOMM project (789340).

Conflict of Interest

All authors have no conflicts of interest.

Received: ((will be filled in by the editorial staff))
Revised: ((will be filled in by the editorial staff))
Published online: ((will be filled in by the editorial staff))

Reference

[1] a) A. S. Roberts, A. Pors, O. Albrektsen, S. I. Bozhevolnyi, *Nano Lett.* **2014**, 14, 783; b) C. U. Hail, G. Schnoering, M. Damak, D. Poulikakos, H. Eghlidi, *ACS Nano* **2020**, 14, 1783; c) Y. Bao, Y. Yu, H. Xu, C. Guo, J. Li, S. Sun, Z.-K. Zhou, C.-W. Qiu, X.-H. Wang, *Light Sci. Appl.* **2019**, 8, 1.
[2] W. Yang, S. Xiao, Q. Song, Y. Liu, Y. Wu, S. Wang, J. Yu, J. Han, D. P. Tsai, *Nat. Commun.* **2020**, 11, 1864.
[3] a) A. M. Shaltout, J. Kim, A. Boltasseva, V. M. Shalaev, A. V. Kildishev, *Nat. Commun.* **2018**, 9, 2673; b) K.

Kumar, H. Duan, R. S. Hegde, S. C. Koh, J. N. Wei, J. K. Yang, *Nat. Nanotechnol.* **2012**, 7, 557; c) T. Chen, B. M. Reinhard, *Adv. Mater.* **2016**, 28, 3522; d) N. J. Greybush, K. Charipar, J. A. Geldmeier, S. J. Bauman, P. Johns, J. Naciri, N. Charipar, K. Park, R. A. Vaia, J. Fontana, *ACS Nano* **2019**, 13, 3875; e) X. Cui, X. Zhu, L. Shao, J. Wang, A. Kristensen, *Adv. Opt. Mater.* **2020**, 8, 1901605; f) J. Zhao, M. Qiu, X. Yu, X. Yang, W. Jin, D. Lei, Y. Yu, *Adv. Opt. Mater.* **2019**, 7, 1900646; g) S. Wu, Y. Ye, H. Duan, Y. Gu, L. Chen, *Adv. Opt. Mater.* **2019**, 7, 1801302; h) J. S. Lee, J. Y. Park, Y. H. Kim, S. Jeon, O. Ouellette, E. H. Sargent, D. H. Kim, J. K. Hyun, *Nat. Commun.* **2019**, 10, 4782; i) Y. J. Kim, Y. J. Yoo, G. J. Lee, D. E. Yoo, D. W. Lee, V. Siva, H. Song, I. S. Kang, Y. M. Song, *ACS Appl. Mater. Interfaces* **2019**, 11, 11849.

[4] a) L. Salomon, F. Grillot, A. V. Zayats, F. de Fornel, *Phys. Rev. Lett.* **2001**, 86, 1110; b) S. Sun, Z. Zhou, C. Zhang, Y. Gao, Z. Duan, S. Xiao, Q. Song, *ACS Nano* **2017**, 11, 4445; c) H. Wang, X. Wang, C. Yan, H. Zhao, J. Zhang, C. Santschi, O. J. F. Martin, *ACS Nano* **2017**, 11, 4419; d) Y. Kim, K. Jung, J. Cho, J. K. Hyun, *ACS Nano* **2019**, 13, 10717.

[5] a) A. P. Ravishankar, M. A. van Tilburg, F. Vennberg, D. Visser, S. Anand, *Nanophotonics* **2019**, 8, 1771; b) B. Yang, W. Liu, Z. Li, H. Cheng, S. Chen, J. Tian, *Adv. Opt. Mater.* **2018**, 6, 1701009; c) S. Sun, W. Yang, C. Zhang, J. Jing, Y. Gao, X. Yu, Q. Song, S. Xiao, *ACS Nano* **2018**, 12, 2151; d) X. Duan, N. Liu, *ACS Nano* **2018**, 12, 8817; e) M. L. Tseng, J. Yang, M. Semmlinger, C. Zhang, P. Nordlander, N. J. Halas, *Nano Lett.* **2017**, 17, 6034; f) V. Flauraud, M. Reyes, R. Paniagua-Domínguez, A. I. Kuznetsov, J. Brugger, *ACS Photonics* **2017**, 4, 1913; g) Z. Dong, J. Ho, Y. F. Yu, Y. H. Fu, R. Paniagua-Dominguez, S. Wang, A. I. Kuznetsov, J. K. W. Yang, *Nano Lett.* **2017**, 17, 7620; h) G. Wang, X. Chen, S. Liu, C. Wong, S. Chu, *ACS Nano* **2016**, 10, 1788.

[6] a) J. M. Guay, A. Cala Lesina, G. Cote, M. Charron, D. Poitras, L. Ramunno, P. Berini, A. Weck, *Nat. Commun.* **2017**, 8, 16095; b) M. Ye, L. Sun, X. Hu, B. Shi, B. Zeng, L. Wang, J. Zhao, S. Yang, R. Tai, H. J. Fecht, J. Z. Jiang, D. X. Zhang, *Opt. Lett.* **2015**, 40, 4979.

[7] a) S. Y. Lee, C. Forestiere, A. J. Pasquale, J. Trevino, G. Walsh, P. Galli, M. Romagnoli, L. Dal Negro, *Opt. Express* **2011**, 19, 23818; b) J. Olson, A. Manjavacas, L. Liu, W. S. Chang, B. Foerster, N. S. King, M. W. Knight, P. Nordlander, N. J. Halas, S. Link, *Proc. Natl. Acad. Sci. USA* **2014**, 111, 14348.

[8] C. Ji, S. Acharya, K. Yamada, S. Maldonado, L. J. Guo, *ACS Appl. Mater. Interfaces* **2019**, 11, 29065.

[9] a) D. J. Roth, M. Jin, A. E. Minovich, S. Liu, G. Li, A. V. Zayats, **2020**, 20, 4481; b) R. J. Ng, X. M. Goh, J. K. Yang, *Opt. Express* **2015**, 23, 32597.

[10] M. Song, D. Wang, S. Peana, S. Choudhury, P. Nyga, Z. A. Kudyshev, H. Yu, A. Boltasseva, V. M. Shalaev, A. V. Kildishev, *Appl. Phys. Rev.* **2019**, 6, 041308.

[11] A. E. Minovich, M. Peter, F. Bleckmann, M. Becker, S. Linden, A. V. Zayats, **2017**, 17, 4189.

[12] A. E. Minovich, A. V. Zayats, *ACS Photonics* **2018**, 5, 1755.

[13] a) P. Liu, L. Bai, J. Yang, H. Gu, Q. Zhong, Z. Xie, Z. Gu, *Nanoscale Advances* **2019**, 1, 1672; b) J. W. Stewart, G. M. Akselrod, D. R. Smith, M. H. Mikkelsen, *Adv. Mater.* **2017**, 29, 1602971; c) D. Franklin, Z. He, P. Mastranzo Ortega, A. Safaei, P. Cencillo-Abad, S. T. Wu, D. Chanda, *Proc. Natl. Acad. Sci. USA* **2020**, 117, 13350.

[14] L. Wang, R. J. H. Ng, S. Safari Dinachali, M. Jalali, Y. Yu, J. K. W. Yang, *ACS Photonics* **2016**, 3, 627.

[15] a) A. Murphy, Y. Sonnefraud, A. V. Krasavin, P. Ginzburg, F. Morgan, J. McPhillips, G. Wurtz, S. A. Maier, A. V. Zayats, R. Pollard, *Appl. Phys. Lett.* **2013**, 102, 103103; b) J. McPhillips, A. Murphy, M. P. Jonsson, W. R. Hendren, R. Atkinson, F. Höök, A. V. Zayats, R. J. Pollard, *ACS Nano* **2010**, 4, 2210.

[16] H. Ni, M. Wang, T. Shen, J. Zhou, *ACS Nano* **2015**, 9, 1913.

[17] S. Wu, Y. Ye, Y. Gu, L. Chen, *Opt. Express* **2019**, 27, 9570.

[18] M. A. van de Haar, R. Maas, B. Brenny, A. Polman, *New J. Phys.* **2016**, 18, 043016.

[19] L. Salomon, F. Grillot, A. V. Zayats, F. de Fornel, *Phys. Rev. Lett.* **2001**, 86, 1110.

[20] M. W. Knight, N. S. King, L. Liu, H. O. Everitt, P. Nordlander, N. J. Halas, *ACS Nano* **2014**, 8, 834.

[21] a) G. V. Odintsova, E. A. Vlasova, Y. M. Andreeva, M. K. Moskvin, A. S. Krivonosov, E. V. Gorbunova, D. V. Pankin, O. S. Medvedev, M. M. Sergeev, N. N. Shchedrina, D. S. Lutoshina, V. P. Veiko, *Opt. Express* **2019**, 27, 3672; b) H. Liu, H. Yang, Y. Li, B. Song, Y. Wang, Z. Liu, L. Peng, H. Lim, J. Yoon, W. Wu, *Adv. Opt. Mater.* **2019**, 7, 1801639.

[22] M. Abdolahi, H. Jiang, B. Kaminska, *Nanotechnology* **2019**, 30, 405301.

[23] a) S. D. Rezaei, J. Ho, A. Naderi, M. T. Yaraki, T. Wang, Z. Dong, S. Ramakrishna, J. K. W. Yang, *Adv. Opt. Mater.* **2019**, 7, 1900735; b) D. Chen, T. Wang, G. Song, Y. Du, J. Lv, X. Zhang, Y. Li, L. Zhang, J. Hu, Y. Fu, R. Jordan, *ACS Appl. Mater. Interfaces* **2019**, 11, 41668.

[24] H. Jiang, B. Kaminska, H. Porras, M. Raymond, T. Kapus, *Adv. Opt. Mater.* **2019**, 7, 1900237.

[25] C. Williams, G. S. D. Gordon, T. D. Wilkinson, S. E. Bohndiek, *ACS Photonics* **2019**, 6, 3132.

[26] B. Hatton, L. Mishchenko, S. Davis, K. H. Sandhage, J. Aizenberg, *Proc. Natl. Acad. Sci. USA* **2010**, 107,

10354.

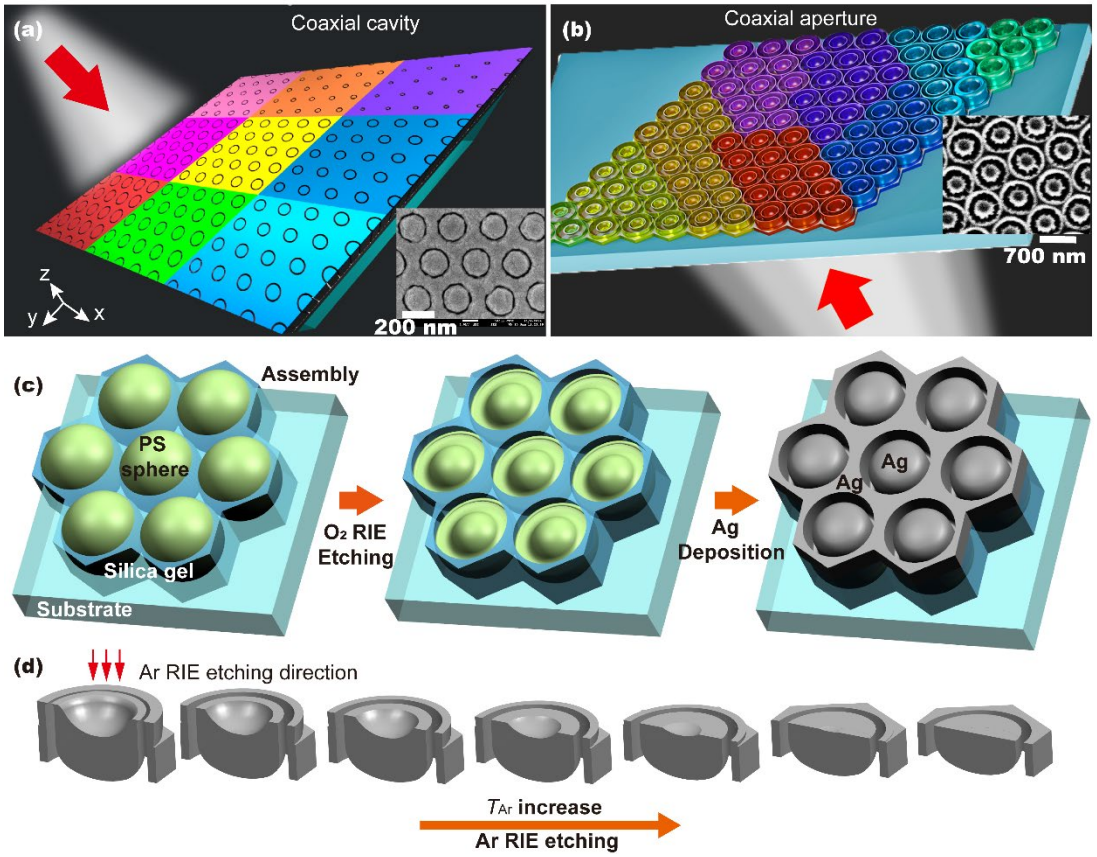

Figure 1. (a) Schematic diagram of the coaxial nanocavity arrays with various parameters producing coloring. Insert: An SEM image of the coaxial nanocavity array with R = 100 nm, W = 10 nm, H = 100 nm, d = 70 nm, P = 250 nm (compare with the final fibrication stage in (c)). (b) Schematic diagram of the coaxial nanoaperture arrays. Inset: An SEM image of the nanoaperture array with R = 280 nm, W = 100 nm, H = 150 nm, d = 100 nm and P = 690 nm (compare with unit cell images at short T_{Ar} times in (d)). (c) Schematic of the fabrication process workflow for the coaxial cavity array. (d) Morphology evolution of the coaxial nanoaperture under Ar milling with increasing time T_{Ar}. Red arrows indicate RIE milling direction. See Methods for details.

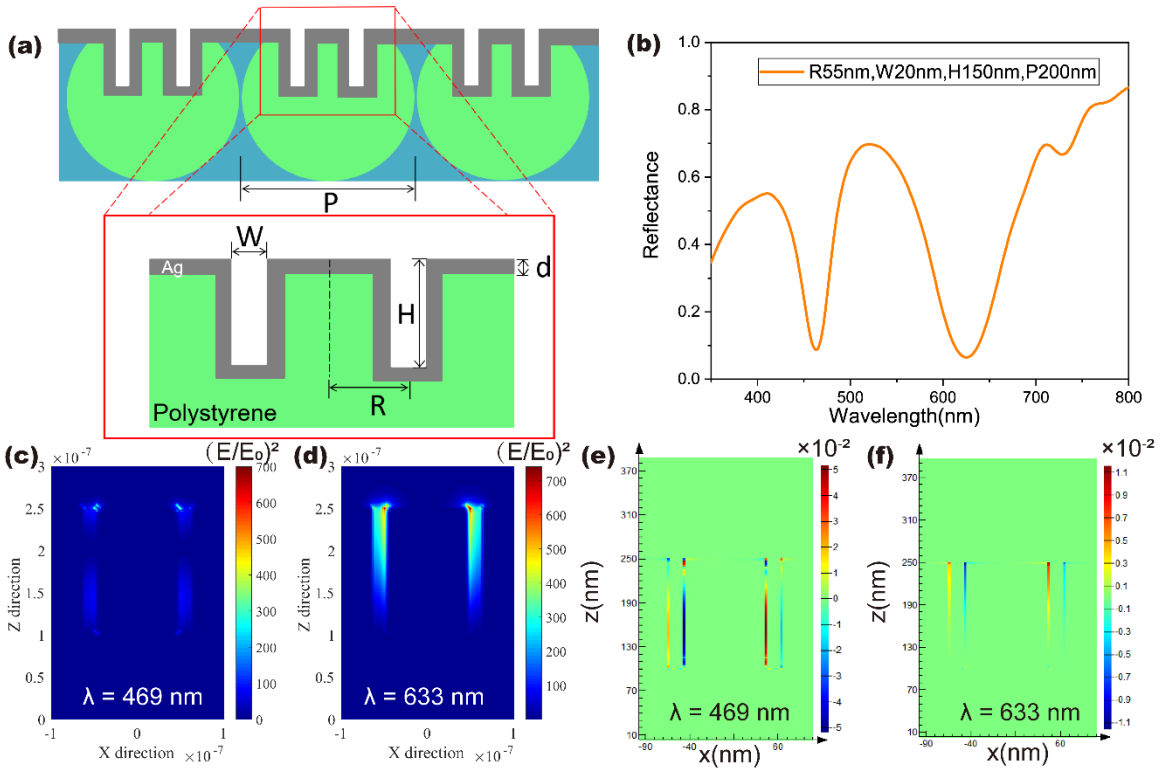

Figure 2. (a) An idealized unit-cell cross-section of coaxial nanocavities with indicated geometrical parameters. (b) Typical simulated reflection spectrum of a coaxial nanocavity array with R = 55 nm, W = 20 nm, H = 150 nm and P = 200 nm. (c,d) Electric field intensity and (e,f) charge distributions in xz-plane at 469 nm and 633 nm wavelengths, corresponding to the reflection dips in (b).

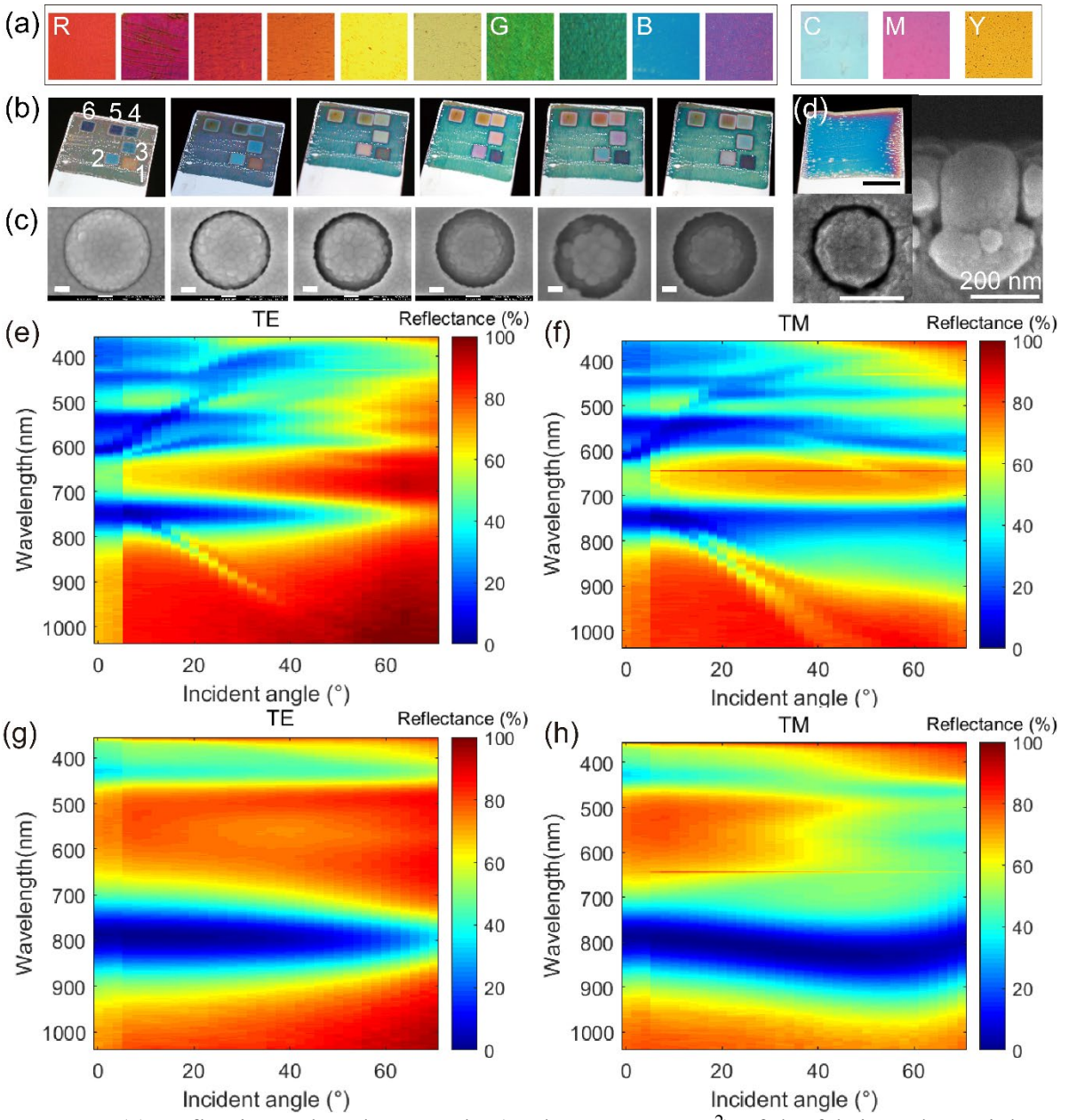

Figure 3. (a) Reflection color photographs (each area 1×1 mm^2) of the fabricated coaxial nanocavity arrays with structural parameters: P = 690 nm, W, H and R are simultaneously varied from 20 to 100 nm, from 100 nm to 400 nm and from 200 nm to 300 nm, respectively, during the fabrication process. (b) Color photographs of six coaxial array areas with various initial states after RIE (marked with 1–6 on the left image) at subsequent stages of silver film deposition (images left to right). The initial geometrical parameters for structures 1–6 in are: 1) R = 325 nm, W = 30 nm and H = 30 nm; 2) R = 310 nm, W = 60 nm and H = 58 nm; 3) R = 295 nm, W = 90 nm and H = 86 nm; 4) R = 280 nm, W = 120 nm and H = 114 nm; 5) R = 265 nm, W = 150 nm and H = 142 nm; 6) R = 250 nm, W = 180 nm and H = 170 nm; which corresponds to a simultaneous variation of the parameters from sample 1 to sample 6 with a step $\Delta R \approx 15$ nm decrease, together with $\Delta H \approx 28$ nm and $\Delta W \approx 30$ nm increases; P = 690 nm is fixed for all 6 samples. Size of each square is 2 mm × 2 mm. Photographs from left to right demonstrate the coloring of the structures with a continuously increased thickness of a sputtered Ag film d from 25 nm (first image on the left) to 150 nm (last image on the right) in

a step of ~ 25 nm, corresponding to simultaneous decreases of ΔR = ~ 6 nm and ΔW = ~ 12 nm and increase of ΔH = ~ 25. (c) SEM images of coaxial nanocavity arrays in areas 1–6 marked in (b) after sputtering 150 nm thick Ag film. Scale bars are 100 nm in all the images. (d) Optical and SEM images of the experimentally produced coaxial nanocavity arrays with R = 105 nm, W = 12 nm, H = 100 nm and P = 250 nm. The scale bar is 5 mm in CCD image and 200 nm in SEM images. (e–h) Experimentally measured angle-resolved reflection spectra (0–70º) of coaxial nanocavity arrays for (e,g) TE- and (f,h) TM-polarized incident light for the samples with structural parameters: (e,f) R = 250 nm, W = 75 nm, H = 375 nm, P = 690 nm, d = 225 nm and (g,h) R = 100 nm, W =15 nm, H = 100 nm, P = 250 nm and d = 70 nm. The abrupt change at 5º is due to an unavoidable minor change of the light spot position at small angles.

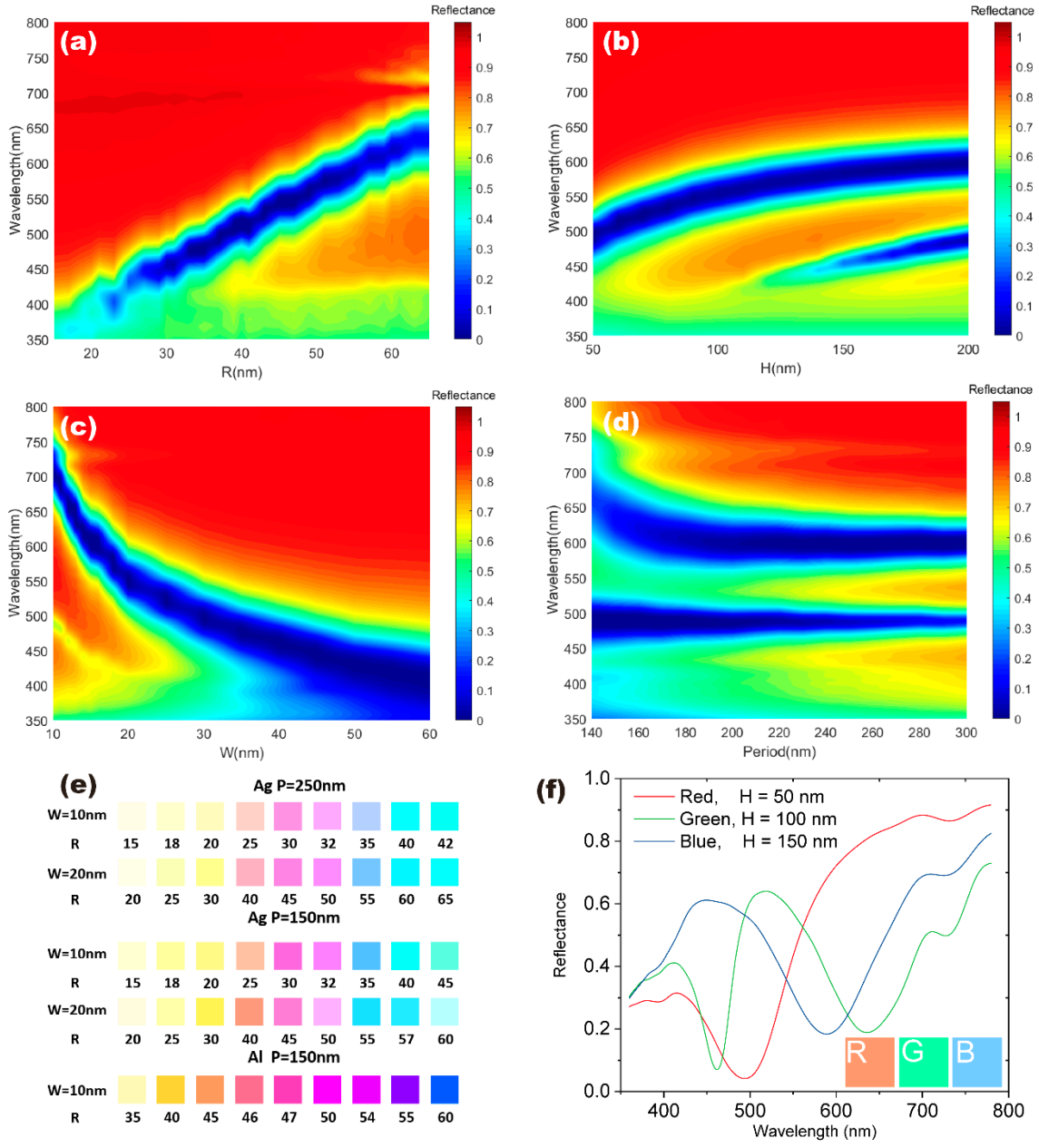

Figure 4. Numerically simulated reflection spectra for (a-d) different (a) radia *R,* (b) heights *H,* (c) gap widths *W* and (d) periodicities *P* for the coaxial nanocavity arrays in an Ag film. The fixed parameters (set of three in each case) in (a–d) are *R* = 50 nm, *W* = 20 nm, *H* = 100 nm and *P* =250 nm except for (d) where *H* = 200 nm. (e) CMY color pallet produced by the color of coaxial nanocavity arrays with varied *R, W* and material composition, but with same *H* = 100 nm, obtained using numerical simulations (see Methods). (f) RGB color pallet realized by varying the nanocavity height *H* with the corresponding reflection spectra *W* =20 nm, *R*=51 nm and *P* = 150 nm.

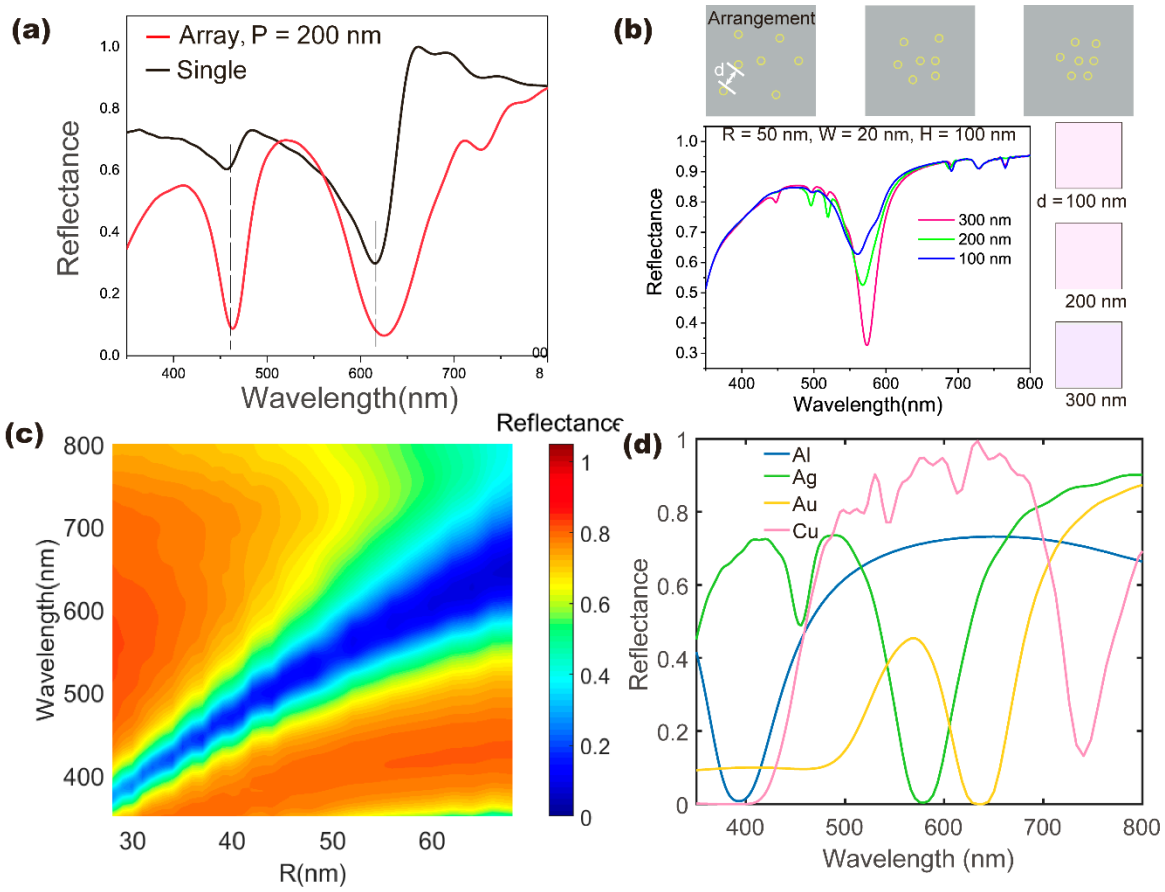

Figure 5. (a) Comparison between the numerically simulated reflection spectra of periodic Ag coaxial nanocavity array (*R* = 55 nm, *W* =20 nm, *H*=150 nm, *P* = 200 nm) and a single coaxial nanocavity with *R* = 55 nm, *W* =20 nm, *H*=150 nm. (b) Schematic diagram of coaxial nanocavities located at random positions with average distances about 300 nm, 200 nm and 100 nm, together with numerically simulated reflection spectra of the random arrays presented in the top line. On the basis of the simulated spectra, the colors in the left bottom were obtained. (c) Color management using Al coaxial nanocavity arrays with *R* = 28–68 nm, *W* = 8 nm, *H* = 100 nm and *P* =250 nm; (d) Numerically simulated reflection spectra of the coaxial nanocavity arrays with the same *R* = 35 nm, *W* = 10 nm, *H* = 100 nm, *P* = 150 nm realized with various metallic materials.

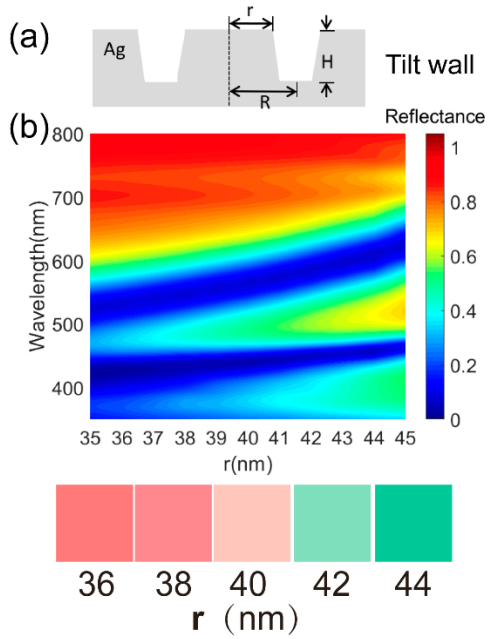

Figure 6. (a) Schematic cross section of a coaxial nanocavity having tilted side walls; (b) Reflection spectra as a function of the inner radius of the coaxial nanocavity *r* (indicated in (a)), varied from 45 nm (vertical walls) to 35 nm (4°tilted walls) with *R* = 55 nm, *W*=20 nm, *H* = 150 nm, *P* = 200 nm, together with the corresponding reflection colors.

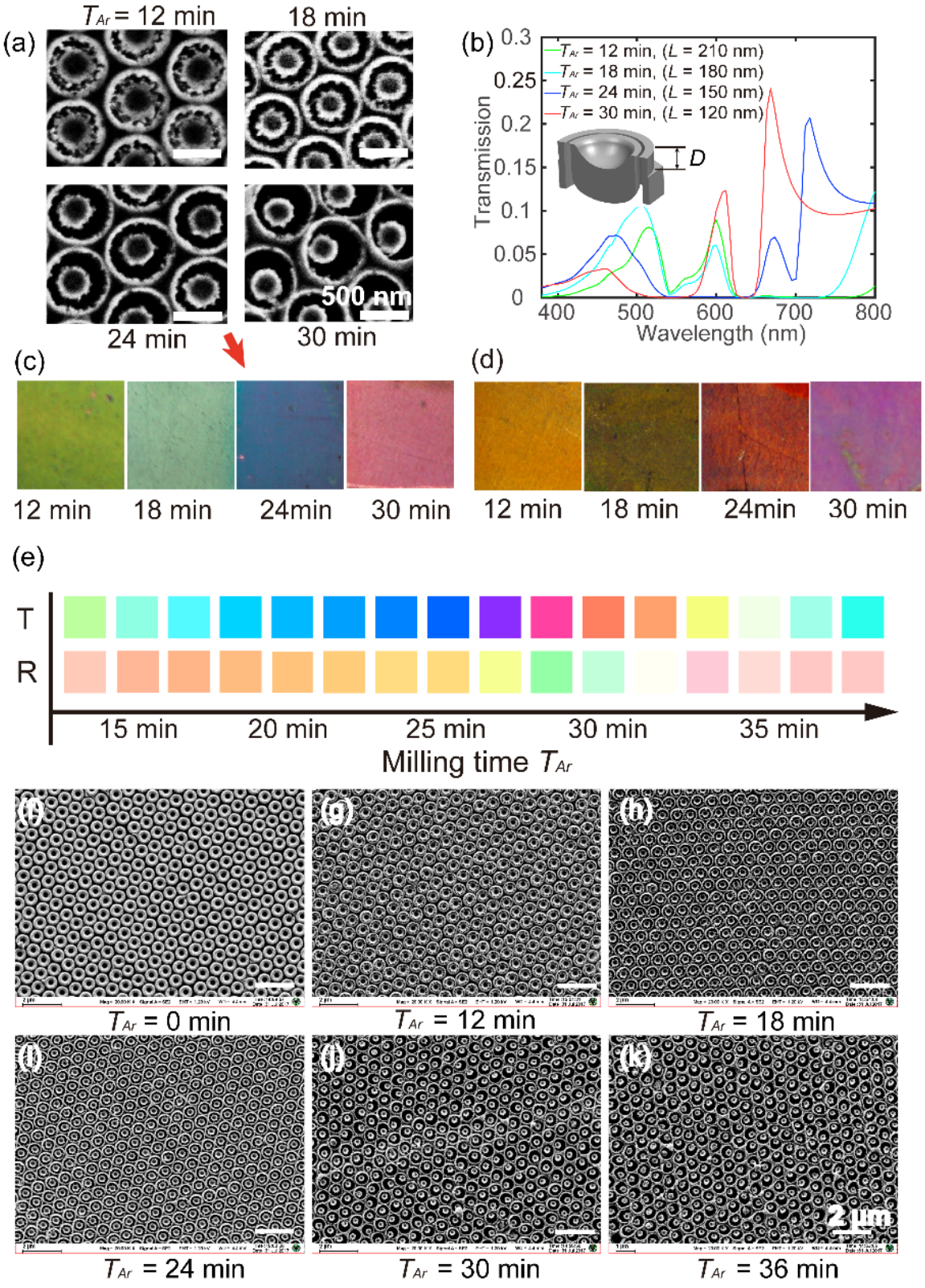

Figure 7. (a) SEM images of the coaxial nanoaperture arrays with an increasing gap width. Scale bar is 500 nm in all images. (b) Simulated transmission spectra of the coaxial nanoaperture arrays (R = 210 nm, W = 160 nm, D =270 nm, P = 690 nm) after various milling times (leading to the decrease of D), calculated for etching speed of ~5 nm/min. The inset shows the geometry of the cross section of the coaxial nanoaperture. Transmission (c) and

reflection (d) images of the coaxial nanoaperture arrays for milling times varied left-to-right: 12, 18, 24 and 30 min. The size of the squares is 2×2 mm^2. (e) Colors of the coaxial nanoaperture arrays in transmission and reflection obtained from numerical simulations. (f–k) SEM images showing the evolution of the nanostructure array during the milling process: (f) initial backside surface morphology of the coaxial nanocavity array, as it is peeled off from the glass substrate, (g–k) after T_{Ar} = 12 (g), 18 (h), 24 (i), 30 (j) and 36 (k) minutes of the reactive ion etching. Scale bar is 2 μm.

An inexpensive and scalable self-assembly technique providing precise color engineering over an entire visible range and offering versatile application opportunities both in reflection and transmission was introduced. The implemented color definition is based on the excitation of localized surface plasmon modes in individual plasmonic nanostructures, which leads to a broad viewing angle response, and offers the possibility of the ultimately small pixel size approaching the diffraction limit.

Haibin Ni,[1,] Alexey V. Krasavin,[2] Lu Zhang, [1] An Ping,[1] Chao Pan,[1] Jianxin Cheng, [1] Ming Wang,[3] Jianhua Chang,[1*] and Anatoly. V. Zayats[2*]*

Self-assembled plasmonic coaxial nanocavities for high-definition broadangle coloring in reflection and transmission